Enhanced Five-Port Ring Circuit Reflectometer for Synthetic Breast Tissue Dielectric Determination

Chia Yew Lee[1], Kok Yeow You[2, *], Tian Swee Tan[1], Yi Lung Then[3],
Yeng Seng Lee[4], Liyana Zahid[5], Wai Leong Lim[5], and Chia Hau Lee[5]

Abstract—In this study, a Six-port Reflectometer (SPR) with dielectric probe sensor is used to predict relative dielectric, ε_r of normal and tumorous breast tissue in frequency range from 2.34 GHz to 3.0 GHz. Other than that, a superstrate with an exterior copper layer is overlaid on the surface of a primitive Five-port Ring Circuit (FPRC), which is also a denominated, enhanced superstrate FPRC. It is the main component of the SPR and is presented in this paper as well. The enhanced superstrate FPRC is capable of improving its operating bandwidth by 26% and shifting the operating centre frequency to a lower value without increasing circuit physical size. The detailed design and characteristics of the FPRC are described here. In addition, the enhanced superstrate FPRC is integrated into the SPR for one-port reflection coefficient measurement. The measurement using the SPR is benchmarked with Agilent's E5071C Vector Network Analyzer (VNA) for one-port reflection coefficient. Maximum absolute mean error of the linear magnitude and phase measurements are recorded to be 0.03 and 5.50°, respectively. In addition, maximum absolute error of the predicted dielectric and loss factor are 1.77 and 0.61, respectively.

1. INTRODUCTION

Breast tumor has been a main cause concerning the loss of life among women (521900 deaths), and it appears to be the most often diagnosed tumor (1676600 additional cases) [1, 2]. Recently, there have been increased cases of breast tumor among men [3]. Although men are less likely to suffer from breast tumor than women, early detection of the breast tumor is important, particularly for treatment of the illness, as the tumor, located at the breast, can only be detected using a sensory device system, and it can be treated before its metastasis [4].

In this study, an integrated SPR with dielectric probe sensor is fabricated and used to determine the dielectric, ε_r of normal and tumorous breast tissue in the frequency range from 2.34 GHz to 3.0 GHz at room temperature. Besides, the probe sensor is fabricated from a 25.3 mm by 25.3 mm square flange, N-type stub contact panel. The synthetic normal and tumorous breast tissue are used as unit under test (UUT) and created by mixing polyethylene glycol mono phenylether (Triton TX-100) with different amounts of water contents proposed by Romeo et al. [5]. The SPR sensor system adopts reflection method for measurements. In addition, the system is assembled and operated based on the five-port ring technique.

The primitive FPRC was proposed by [6] as an SPR for one-port reflection coefficient measurement instead of using commercial VNA. Ideally, it has electrical properties of 120° phase difference between

* Corresponding author: Kok Yeow You (kyyou@fke.utm.my).
[1] Biotechnology and Medical Engineering Department, Universiti Teknologi Malaysia, Skudai, Johor 81310, Malaysia.
[2] Communication Engineering Department, Faculty of Electrical Engineering, Universiti Teknologi Malaysia, Skudai, Johor 81310, Malaysia. [3] Faculty of Engineering, Computing and Science, Swinburne University of Technology Sarawak Campus, Jalan Simpang Tiga, 93300 Kuching, Sarawak, Malaysia. [4] Department of Electronic Engineering Technology, Faculty of Engineering Technology, Univerisiti Malaysia Perlis (UniMAP), Pauh Putra Campus, Arau, Perlis 02600, Malaysia. [5] Computer & Communication Engineering School, Univerisiti Malaysia Perlis (UniMAP), Pauh Putra Campus, Arau, Perlis 02600, Malaysia.

adjacent ports, and the magnitude of transmission coefficient at each receiving port is 6 dB, which can be applied to phase modulator, four-way power divider, and SPR. Nonetheless, the actual FPRC has a phase error compared to the ideal case, which causes poor performance in phase modulator or four-way power divider. However, the wider tolerance of phase error between adjacent ports of the FPRC is allowed for SPR applications [7–9].

The SPR was formed by an FPRC and directional coupler, which is simpler and requires fewer circuit components than other SPR structures [10–12]. Nevertheless, the drawback of the primitive FPRC based SPR is the narrow operating bandwidth device. In fact, the operating bandwidth (BW) improvement for several microstrip-based FPRC has been demonstrated by [13–16]. The most comprehensive analysis for the FPRC was proposed by [17]. Besides, [18] made further improvement on BW of the FPRC by replacing the multi-section transmission line [17] with a taper shape design. However, those improved designs require much bigger physical circuit.

In this study, the BW of the primitive FPRC is widened by overlaying an FR4 superstrate with an exterior copper layer on top of the primitive FPRC. Simultaneously, the centre frequency, f, of the enhanced superstrate FPRC is shifted to a lower value while retaining the circuit board's physical size. The copper layer at exterior surface of the superstrate induces additional parasitic capacitance that affects the wave propagation of the FPRC. An analytical modeling of the enhanced superstrate FPRC is simulated as a guide at pre-fabrication phase. The maximum radiation distance of the FPRC is measured by moving the metal plate away from the surface of the FPRC. The maximum radiation indicates maximum thickness of superstrate in altering characteristics of the FPRC. The enhanced superstrate FPRC is integrated into SPR, its reflection accuracy examined using three unknown loads, and the results are validated by commercial E5071C VNA.

2. ANALYTICAL THEORY OF FPRC

Figure 1 shows a structure of primitive FPRC.
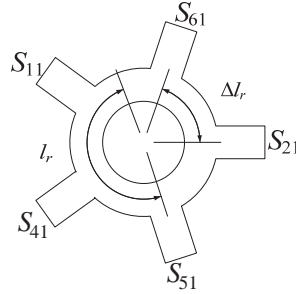
Figure 1. Primitive five-port ring circuit (FPRC).

The ideal reflection and transmission coefficients (S_{11}, S_{21}, S_{41}, S_{51} and S_{61}) for each port of FPRC are expressed in Equations (1) to (3) as [17]:

$$S_{11} = \frac{e^{j\theta_1} + 2(e^{j(\theta_1+\theta+\Delta\theta)} + e^{j(\theta_1+\theta-\Delta\theta)})}{5} \tag{1}$$

$$S_{21} = S_{51} = \frac{e^{j\theta_1} + 2\left\{e^{j(\theta_1+\theta+\Delta\theta)}\cos(2\pi/5) + e^{j(\theta_1+\theta-\Delta\theta)}\cos(4\pi/5)\right\}}{5} \tag{2}$$

$$S_{41} = S_{61} = \frac{e^{j\theta_1} + 2\left\{e^{j(\theta_1+\theta+\Delta\theta)}\cos(4\pi/5) + e^{j(\theta_1+\theta-\Delta\theta)}\cos(2\pi/5)\right\}}{5} \tag{3}$$

where θ and $\Delta\theta$ (in radian) in Equations (1)–(3) can be estimated as [17]:

$$\cos^{-1}\left(\frac{1-5|S_{11}|}{4}\right) \le \Delta\theta \le \cos^{-1}\left(\frac{1+5|S_{11}|}{4}\right) \tag{4}$$

$$\theta = \pi - \cos^{-1}\left[\frac{1-2|S_{11}|^2}{8\cos(\Delta\theta)} + 2\cos(\Delta\theta)\right] \tag{5}$$

In fact, the value of θ_1 is insensitive to S_{11}, S_{21} and S_{41}. Thus, $e^{j\theta_1}$ can be assumed as unity (without any initial phase shift, and $\theta_1 \approx 0$). In this study, Equations (1)–(5) are used as computer-aided design (CAD) tool in order to design the dimensions of the FPRC in conjunction with the microstrip realization equation [19]. Firstly, Equations (1)–(3) are rewritten in frequency domain as [17]:

$$S_{11} = \frac{\left\{ 1 + 2\exp\left[\left(\alpha + j\frac{2\pi f}{c}\sqrt{\varepsilon_{\text{eff}}}\right)(l_r + \Delta l_r)\right] + 2\exp\left[j\frac{2\pi f}{c}\sqrt{\varepsilon_{\text{eff}}}\,(l_r - \Delta l_r)\right] \right\}}{5} \tag{6}$$

$$S_{21} = \frac{\left\{ 1 + 2\exp\left[j\frac{2\pi f}{c}\sqrt{\varepsilon_{\text{eff}}}\,(l_r + \Delta l_r)\right]\cos(2\pi/5) + 2\exp\left[j\frac{2\pi f}{c}\sqrt{\varepsilon_{\text{eff}}}\,(l_r + \Delta l_r)\right]\cos(4\pi/5) \right\}}{5} \tag{7}$$

$$S_{41} = \frac{\left\{ 1 + 2\exp\left[j\frac{2\pi f}{c}\sqrt{\varepsilon_{\text{eff}}}\,(l_r + \Delta l_r)\right]\cos(4\pi/5) + 2\exp\left[j\frac{2\pi f}{c}\sqrt{\varepsilon_{\text{eff}}}\,(l_r + \Delta l_r)\right]\cos(2\pi/5) \right\}}{5} \tag{8}$$

The effective relative permittivity, ε_{eff}, is given as [19]:

$$\varepsilon_{\text{eff}} = \frac{\varepsilon_{r1} + \varepsilon_{r2}}{2} + \frac{\varepsilon_{r1} - \varepsilon_{r2}}{2}\frac{1}{\sqrt{1 + 12d/w}} \tag{9}$$

where ε_{r1} and ε_{r2} are the relative permittivity of substrate and superstrate, respectively. t_s is the thickness of the substrate and w the width of the of the of the copper trace which can be calculated as [19]:

$$\frac{w}{t_s} = \begin{cases} \dfrac{8\exp(A)}{\exp(2A) - 2} & \text{for } \dfrac{w}{d} < 2 \\[2ex] \dfrac{2}{\pi}\left\{ B - 1 - \ln(2B-1) + \dfrac{\varepsilon_{r1} - 1}{2\varepsilon_{r1}}\left[\ln(B-1) + 0.39 - \dfrac{0.61}{\varepsilon_{r1}}\right] \right\} & \text{for } \dfrac{w}{d} > 2 \end{cases} \tag{10}$$

where $A = \frac{Z_o}{60}\sqrt{\frac{\varepsilon_{r1}+1}{2}} + \frac{\varepsilon_{r1}-1}{\varepsilon_{r1}+1}\left(0.23 + \frac{0.11}{\varepsilon_{r1}}\right)$ and $B = \frac{377\pi}{2Z_o\sqrt{\varepsilon_{r1}}}$.

Here, Z_o is the characteristic impedance of the microstrip ring line. At the resonant frequency f_r, the reflection coefficient $|S_{11}| \approx 0$, thus, $\Delta\theta \approx 1.309\,\text{rad}$ (75°) and $\theta \approx 3.142\,\text{rad}$ (180°). The physical length l_r and Δl_r (in meters) in Equations (6)–(8) are estimated as: $l_r = \frac{3.142c}{2\pi f_r\sqrt{\varepsilon_{\text{eff}}}}$ and $\Delta l_r = \frac{1.309c}{2\pi f_r\sqrt{\varepsilon_{\text{eff}}}}$ where c ($\approx 3 \times 10^8\,\text{ms}^{-1}$) is the speed of light in free space.

3. FPRC CONFIGURATION

In this work, three different configurations of FPRC are fabricated and investigated as shown in Figures 2(a), (b) and (c) below.


(a)   (b)   (c)
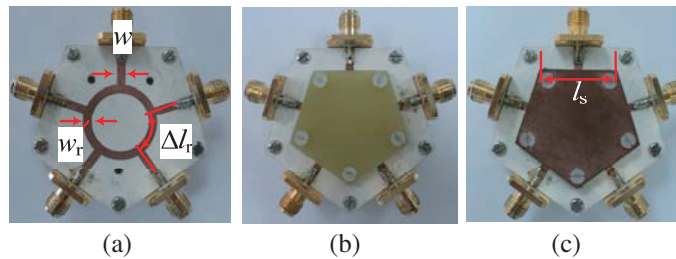
Figure 2. Configuration of (a) primitive, (b) superstrate, and (c) enhanced superstrate FPRCs.

Description of the measurements and performance analysis of the FPRCs in Figures 2(a), (b) and (c) are presented in Sections 3.1 to 3.3, respectively.

3.1. The First Configuration of FPRC (Primitive)

For the first configuration of FPRC in Figure 2(a), the circuit without overlaying any superstrate has an operating resonant frequency, $f_r = 3\,\text{GHz}$, and the ring dimension was printed on a Rogers RO4360 substrate ($\varepsilon_{r1} = 6.15 - \text{j}0.025$, $d = 1.524\,\text{mm}$, and copper thickness $= 17\,\mu\text{m}$). The dimensions of the FPRC was specifically designed to ensure that the value of Z_o was fixed at $45.5\,\Omega$ [17], and the section length Δl_r is required to be equal to $0.211c/(f_r\sqrt{\varepsilon_{eff}})$, in order to provide a matched circuit condition ($S_{11} \approx -\infty\,\text{dB}$ or $S_{11} \approx 0$) at the resonant frequency f_r [17]. Hence, by using Equation (10), the values of w and Δl_r were calculated to be $2.63\,\text{mm}$ and $8.80\,\text{mm}$, respectively.

   The resonant efficiency of the ring at $3\,\text{GHz}$ obtained from measurement ($S_{11} \approx -26\,\text{dB}$) was less ideal than theoretical results ($S_{11} \approx -35\,\text{dB}$), as shown in Figure 3(a), because the conductor loss was not taken into account in theoretical calculation. On the other hand, the measured $|S_{21}|$, $|S_{41}|$, $|S_{51}|$, $|S_{61}|$ and phase difference between adjacent ports deviate slightly from the calculation as shown in Figures 3(b) and (c), which was mainly caused by the abrupt transmission line bend at the junction between the feedline and the ring.
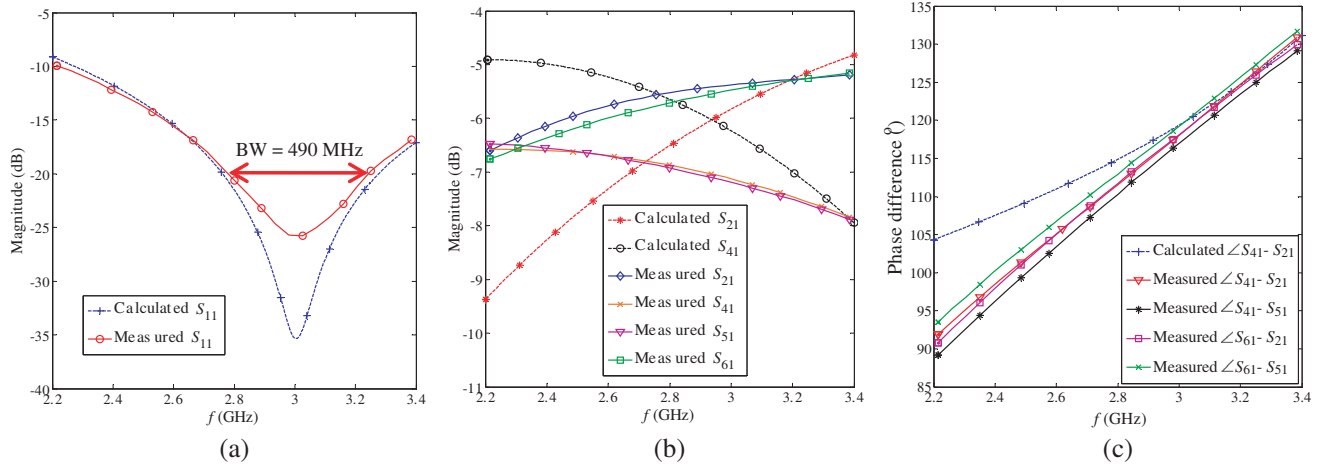
Figure 3. Measurement and calculation of primitive FPRC (a) S_{11} magnitude, (b) S_{21}, S_{41}, S_{51}, and S_{61} magnitude, (c) phase difference.

3.2. Second Configuration of FPRC (Superstrate)

To form the second configuration of FPRC, the primitive FPRC was overlaid with a layer of FR4 superstrate ($\varepsilon_{r2} = 4.4 - \text{j}0.088$) as shown in Figure 2(b). The higher dielectric value of FR4 causes some microstrip propagation delay, as given by Equation (11) below:

$$\lambda_g = \frac{c}{f\sqrt{\varepsilon_{eff}}}. \tag{11}$$

where c is the speed of light in free space ($299792458\,\text{ms}^{-1}$), λ_g the wavelength of wave propagate in FPRC, and ε_{eff} the effective permittivity obtained from Equation (11). ε_{eff} is higher for the second FPRC configuration than the first one and makes the wavelength λ_g shorter. Hence, the new wavelength λ_g that complies with the phase shift characteristic at a fixed physical microstrip line is given resonant condition at a lower frequency of $2.66\,\text{GHz}$.

   The FR4 thickness is determined by adjusting the metal plate away from the surface of the primitive FPRC until return loss $|S_{11}|$ at port-1 becomes constant. The $|S_{11}|$ was measured for different increasing thicknesses t_g of the air gap between the metal plate and the top surface of FPRC. Figure 4 shows a plotted graph of $|S_{11}|$ versus t_g, in which the effect of the metal plate to FPRC was diminished after exceeding $1.4\,\text{mm}$ and $3.8\,\text{mm}$ at $2.69\,\text{GHz}$ and $3.06\,\text{GHz}$, respectively. Clearly, the radiated fields were concentrated on the FPRC and decayed rapidly from FPRC. Hence, $3.2\,\text{mm}$ of FR4 superstrate was used, and it was sufficient to cover the radiated fields from the FPRC over the operating frequency range.
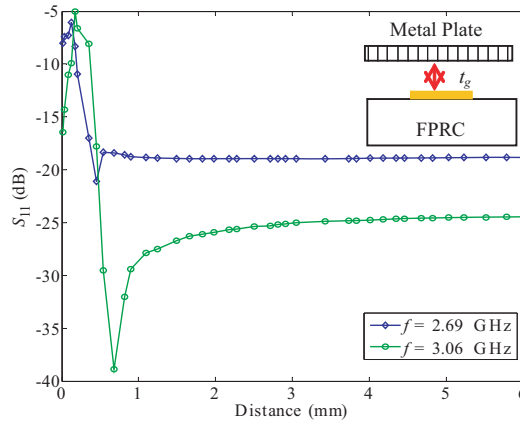
Figure 4. Variation in magnitude of $|S_{11}|$ with metal plate distance, t_g at frequency 2.69 GHz and 3.06 GHz.

There are some deviations between the actual measurement and theoretical calculation, as shown in Figures 5(a) to (c), which were induced by the same factors, as mentioned in Section 3.1. The slight variation of resonant frequency between measurement and theoretical calculation could be due to the existence of small air gap between the surfaces of the substrate and superstrate.
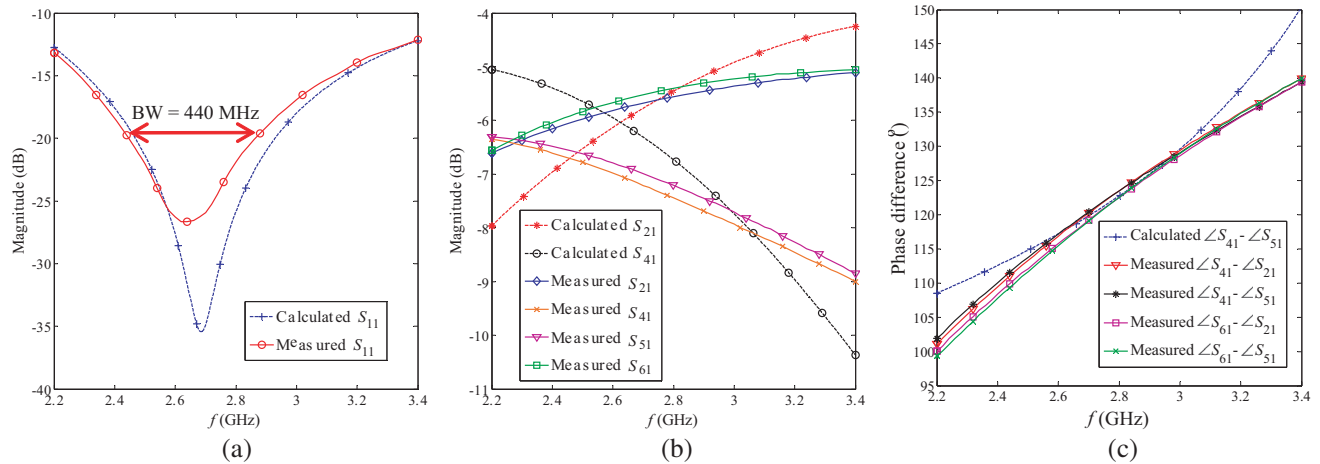

Figure 5. Measurement and theoretical calculation of superstrate FPRC. (a) S_{11} magnitude, (b) S_{21}, S_{41}, S_{51}, and S_{61} magnitude, (c) phase difference.

3.3. Third FPRC Configuration (with Enhanced Superstrate)

In the third configuration of FPRC, the superstrate FPRC was overlaid with a copper layer at exterior surface, as shown in Figure 2(c). The additional parasitic capacitance is introduced to the FPRC, where polarity of the parasitic "capacitor" swap continuously as the continuous wave propagates through the sandwiched medium, as shown in Figure 6. It should be noted that the exterior copper layer is not connected to the ground.

The virtual parasitic capacitor may induce the dual resonant phenomena at about 2.5 GHz and 2.85 GHz where the adjacency between the resonances is close enough to overlap and subsequently improves the BW of FPRC. The variation of S-parameter due to positive capacitance polarity can be calculated with Equations (12) to (14), while the negative capacitance polarity can be calculated with Equations (15) to (17). The actual S-parameter can be calculated by substituting Equations (12) to
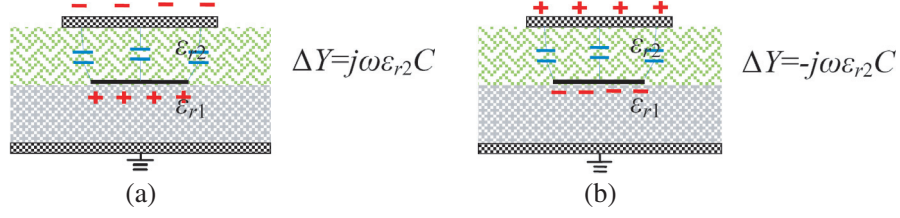
Figure 6. Parasitic capacitance, C due to (a) positive, (b) negative polarizations.

(17) into Equations (18) to (20). The value of the parasitic capacitance C can be calculated using Equation (21). Furthermore, the adjacency between the two resonances can be altered by changing the thickness of the superstrate.

$$S'_{11} = \frac{1 - [(1 - S_{11})/(1 + S_{11})] + j\omega\varepsilon_{r2}C}{1 + [(1 - S_{11})/(1 + S_{11})] - j\omega\varepsilon_{r2}C} \tag{12}$$

$$S'_{21} = \frac{1 - [(1 - S_{21})/(1 + S_{21})] + j\omega\varepsilon_{r2}C}{1 + [(1 - S_{21})/(1 + S_{21})] - j\omega\varepsilon_{r2}C} \tag{13}$$

$$S'_{41} = \frac{1 - [(1 - S_{41})/(1 + S_{41})] + j\omega\varepsilon_{r2}C}{1 + [(1 - S_{41})/(1 + S_{41})] - j\omega\varepsilon_{r2}C} \tag{14}$$

$$S''_{11} = \frac{1 - [(1 - S_{11})/(1 + S_{11})] - j\omega\varepsilon_{r2}C}{1 + [(1 - S_{11})/(1 + S_{11})] + j\omega\varepsilon_{r2}C} \tag{15}$$

$$S''_{21} = \frac{1 - [(1 - S_{21})/(1 + S_{21})] - j\omega\varepsilon_{r2}C}{1 + [(1 - S_{21})/(1 + S_{21})] + j\omega\varepsilon_{r2}C} \tag{16}$$

$$S''_{41} = \frac{1 - [(1 - S_{41})/(1 + S_{41})] - j\omega\varepsilon_{r2}C}{1 + [(1 - S_{41})/(1 + S_{41})] + j\omega\varepsilon_{r2}C} \tag{17}$$

where S_{11}' and S''_{11} are the reflection coefficients due to the positive and negative capacitor polarities respectively. S_{21}' and S_{41}' are the transmission coefficients due to positive capacitor polarity, while S''_{21} and S''_{41} are the transmission coefficients due to negative capacitor polarity.

$$S_{11}^{eff} = \frac{S'_{11}S''_{11}}{S'_{11} + S''_{11}} \tag{18}$$

$$S_{21}^{eff} = \frac{S'_{21} + S''_{21}}{2} \tag{19}$$

$$S_{41}^{eff} = \frac{S'_{41} + S''_{41}}{2} \tag{20}$$

where S_{11}^{eff} is the actual reflection coefficient, and S_{21}^{eff} and S_{41}^{eff} are the actual transmission coefficients.

$$C = \varepsilon_o\varepsilon_{r2}\frac{\pi\left(\left(\frac{5\Delta l_r}{2\pi} + \frac{w}{2}\right)^2 - \left(\frac{5\Delta l_r}{2\pi} - \frac{w}{2}\right)^2\right)}{t_s} \tag{21}$$

where ε_o ($\approx 8.8542 \times 10^{-12}\,\mathrm{F\,m^{-1}}$) is the permittivity of free space. t_s is the thickness of the superstrate as shown in Figure 7.

The measurement of phase differences between adjacent ports and transmission coefficient appear slightly distorted from theoretical calculation, as shown in Figures 8(a) to (c), which might be due to small portion wave loss penetrating through the thin exterior copper layer.

Both superstrate and enhanced superstrate FPRC have lower operating centre frequency than the primitive FPRC as expected. Additionally, the enhanced superstrate FPRC has broader BW (26% BW) than primitive FPRC (16% BW) as well as superstrate FPRC (16% BW). Further detailed characteristics of the three FPRCs are tabulated in Table 1.
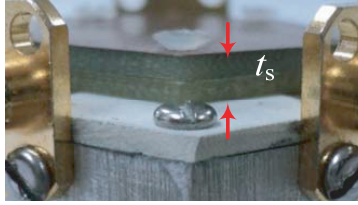
Figure 7. Thickness of the superstrate.

Table 1. Characteristics of primitive, superstrate, and enhanced superstrate FPRC.

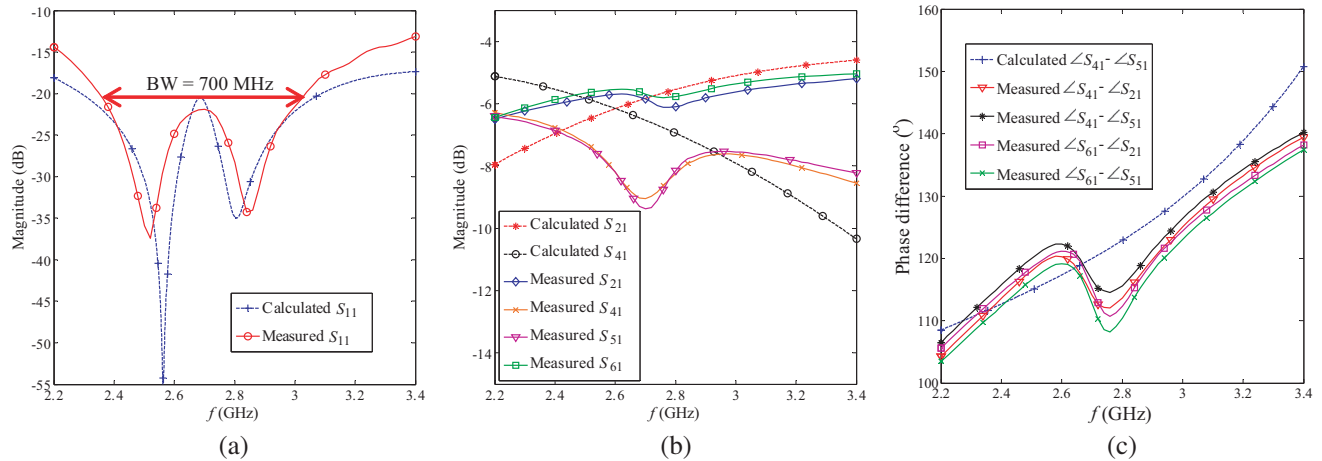| Performance	FPRC		
	Primitive (Configuration 1)	Superstrate (Configuration 2)	Enhanced superstrate (Configuration 3)
Bandwidth, BW (MHz)	490	440	700
Operating frequency (GHz)	2.75–3.24	2.44–2.88	2.34–3.04
Transmission unbalanced (dB)	1.6	1.4	3.4
Phase unbalanced (°)	11.2	10.1	11.8

(a)   (b)   (c)

Figure 8. Measurement and theoretical calculation of enhanced superstrate FPRC. (a) S_{11} magnitude, (b) S_{21}, S_{41}, S_{51}, and S_{61} magnitude, (c) phase difference.

4. INTEGRATION OF FPRC IN SPR SYSTEM

The enhanced superstrate FPRC was integrated into the SPR system to examine its performance using E5071C VNA. The system consists of a Lab Brick LSG-602 signal generator, four LTC2400 24-bit ADCs, four ADA-4528 chopper amplifiers, four SHX-803-S-4 Schottky diode detectors, a PE-2214 10-dB directional coupler, an ATmega328 microcontroller, a PC, and an enhanced superstrate FPRC, as shown in Figure 9 below. Port 1 was used as input port while Port 2 was used as the measurement port. The rest of the ports (port 4 to 6) were used as detection ports for the Schottky diode detectors.

The operating frequency and source power level from the signal generator were controlled by PC through USB interface. The signal source was fed into the directional coupler, and a part of the signal was fed into port 3 as a reference incident signal. Then, transmission signal from directional coupler at port 1 was fed into the enhanced superstrate FPRC. The output signals at port 3 to 6 were detected by the Schottky diode detectors that provide output voltages. However, if current from the detectors is too low for the ADCs, inaccurate output voltages may be produced. Thus, chopper amplifiers were inserted
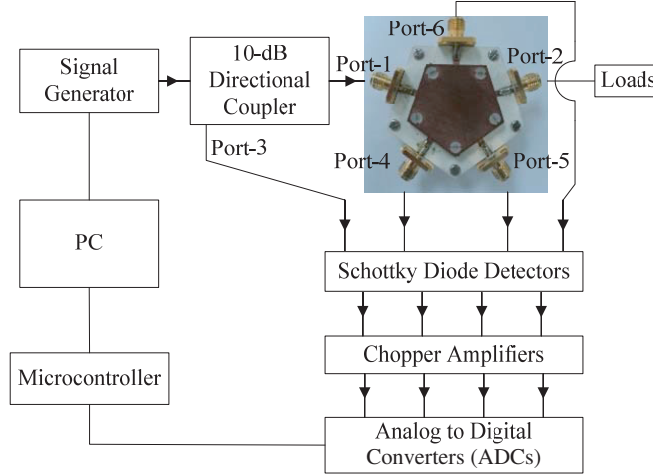
Figure 9. Configuration of the SPR.

among diode detectors and ADCs that act as a buffer, which increases the diode detector current to eliminate inaccurate voltage measurement. The ADCs convert the analog output voltages into their digital representation, which could be computed by the PC. Nevertheless, the ADCs only provide Serial Peripheral Interface (SPI) for data transmission. Thus, the microcontroller was utilized to receive data from the ADCs through SPI and transmitted back to the PC through USB interface.

## 5. SIX-PORT CALIBRATION PROCEDURE

There are two calibrations needed, i.e., diode detector and SPR calibrations. Both calibration procedures are separated into five sub-processes as follows:

(i) The nonlinear diode detector was calibrated using the method proposed by [20].

(ii) The six-port to four-port reduction technique was applied, which converted actual reflectometer to a reflectometer in w-plane and error box as proposed by [21].

(iii) The initial constant values of the reflectometer in w-plane were estimated using mathematical routines reported by [22–24].

(iv) The acquired initial constant was optimized again using the optimization mathematical model by [25].

(v) Finally, the calibration process using three standard kits (open-circuit, short-circuit and match load) was done to obtain actual complex reflection coefficient at measurement port (i.e., port-2) [21].

6. SPR PERFORMANCE EVALUATION

The SPR system was evaluated using three unknown loads, namely a 50FP-003-H6 3-dB attenuator, an MCL BW-S6W2 6-dB attenuator, and a 2082-6193-10 10-dB attenuator, respectively. The comparisons of magnitude $|S_{11}|$ and phase ϕ of the reflection coefficient between SPR and E5071C VNA are shown in Figure 10 below. Besides, mean magnitude errors, $\Delta|S_{11}|$ between E5071C VNA and SPR for the first, second and third loads are 0.03, 0.03, and 0.01, respectively, whereas mean phase errors $\Delta\phi$ between E5071C VNA and SPR for the first, second and third loads are 4.54°, 3.38°, and 5.50°, respectively. Deviation of load 1's magnitude between SPR and VNA in Figure 10(a) seems noticeable. This might be due to the nonlinear characteristics of the Schottky diode detectors that cause error in the power measurement at ports 3 to 6. On the other hand, measurements of the three loads using FieldFox N9952A, namely moderate cost VNA instrument are presented in Figure 10 as a guideline for potential error measurement. The maximum magnitude errors of the first to third loads between E5071C VNA and N9952A VNA are 0.02, 0.01, and 0.01, respectively, while the maximum phase errors of the first to third loads between the E5071C VNA and N9952A VNA are 1.96°, 2.47°, and 3.37°, respectively.
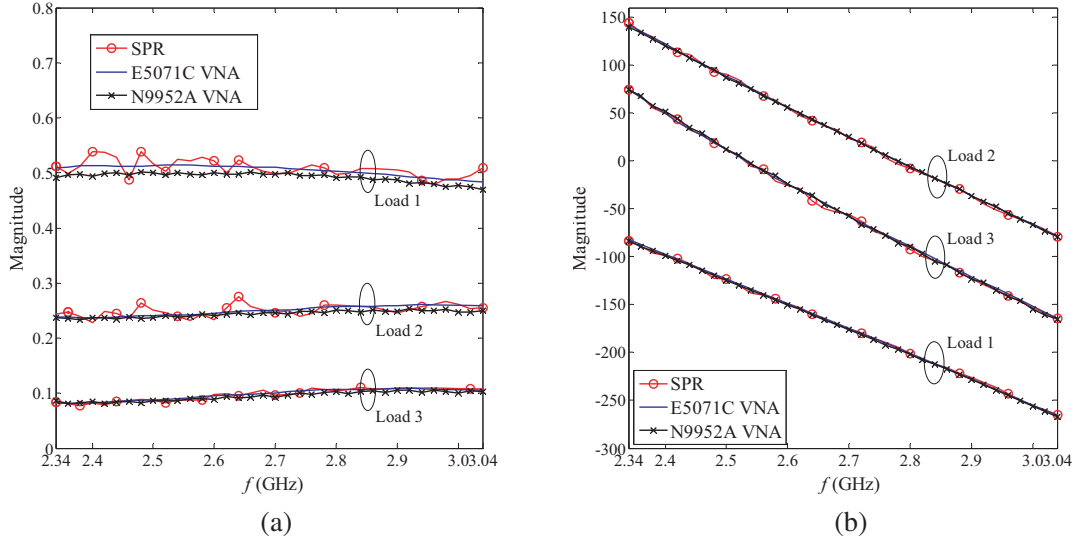
Figure 10. Measurement, (a) magnitude, (b) phase of SPR, E5071C VNA and N9952A VNA with three unknown loads.

7. APPLICATION OF SPR FOR DIELECTRIC PROPERTY DETERMINATION

In this section, the dielectric determination using fully-integrated SPR with the dielectric probe is presented. Besides, the dielectric measurement using commercial E5071C VNA with Agilent 85070E dielectric probe was included as a reference for the dielectric. Here, N9952A VNA measurements are shown in Figures 11(a)–(e) as a guideline for potential errors. During measurements, the dielectric probe was immersed into synthetic breast tissue samples.

The solution based synthetic breast samples by Romeo et al. [5] was used in the dielectric determination, which consists of a different ratio of water and TX-100. Symbol T represents the solution of tumorous breast tissue while symbols $B1$, $B2$, and $B3$ represent the solutions of three categories of normal breast tissue.

The dielectric probe connected to SPR measurement port has characteristic impedance $Z_o = [60 \times \ln(b_c/a_c)/\sqrt{\varepsilon_c}] = 50\,\Omega$ [19]. The inner conductor, $a_c = 1.45\,\text{mm}$, the outer conductor, $b_c = 4.75\,\text{mm}$, the dielectric medium between inner and outer conductors, $\varepsilon_c = 2.06$. Other than that the dielectric and loss factor of the samples can be determined using the bilinear equation [26] below:

$$\varepsilon_r = -\left(\frac{A\varepsilon_{r\_e}\varepsilon_{r\_p} + B\varepsilon_{r\_w}\varepsilon_{r\_e} + C\varepsilon_{r\_p}\varepsilon_{r\_w}}{A\varepsilon_{r\_w} + B\varepsilon_{r\_p} + C\varepsilon_{r\_e}} \right) \qquad (22)$$

where $A = (\Gamma_{meas} - \Gamma_W) \times (\Gamma_E - \Gamma_P)$, $B = (\Gamma_{meas} - \Gamma_P) \times (\Gamma_W - \Gamma_E)$, and $C = (\Gamma_{meas} - \Gamma_E) \times (\Gamma_P - \Gamma_W)$. Γ_W, Γ_P and Γ_E are the measured reflection coefficients of the water, propan-2-ol, and ethanol at the SPR measurement port.

Γ_{meas} is the measured reflection coefficient, while ε_{r_w}, ε_{r_p} and ε_{r_e} are the known relative permittivity for air, propan-2-ol and ethanol at 25°C, obtained from [27].

The maximum errors between actual measured and reference magnitude for samples T, $B1$, $B2$, and $B3$ are 0.02, 0.02, 0.01 and 0.02, respectively. The maximum errors between reference and N9952A VNA magnitude for samples T, $B1$, $B2$, and $B3$ are 0.04, 0.06, 0.04, and 0.02 respectively. $B3$ sample has the highest magnitude while $B2$ has the lowest magnitude among all the samples. By observation, all of the samples' magnitudes decrease with the frequency, shown in Figures 11(a)–(d). In addition, Figure 11(a) shows the magnitude value for T sample at 2.45 GHz approximately in range from 0.803 to 0.811. Meanwhile, Figure 11(d) shows that the magnitude value for $B1$ sample is in the range from 0.816 to 0.817 at 2.45 GHz. Clearly, the difference between tumorous and normal synthetic breast tissue samples is differentiable based on the magnitude measurement.
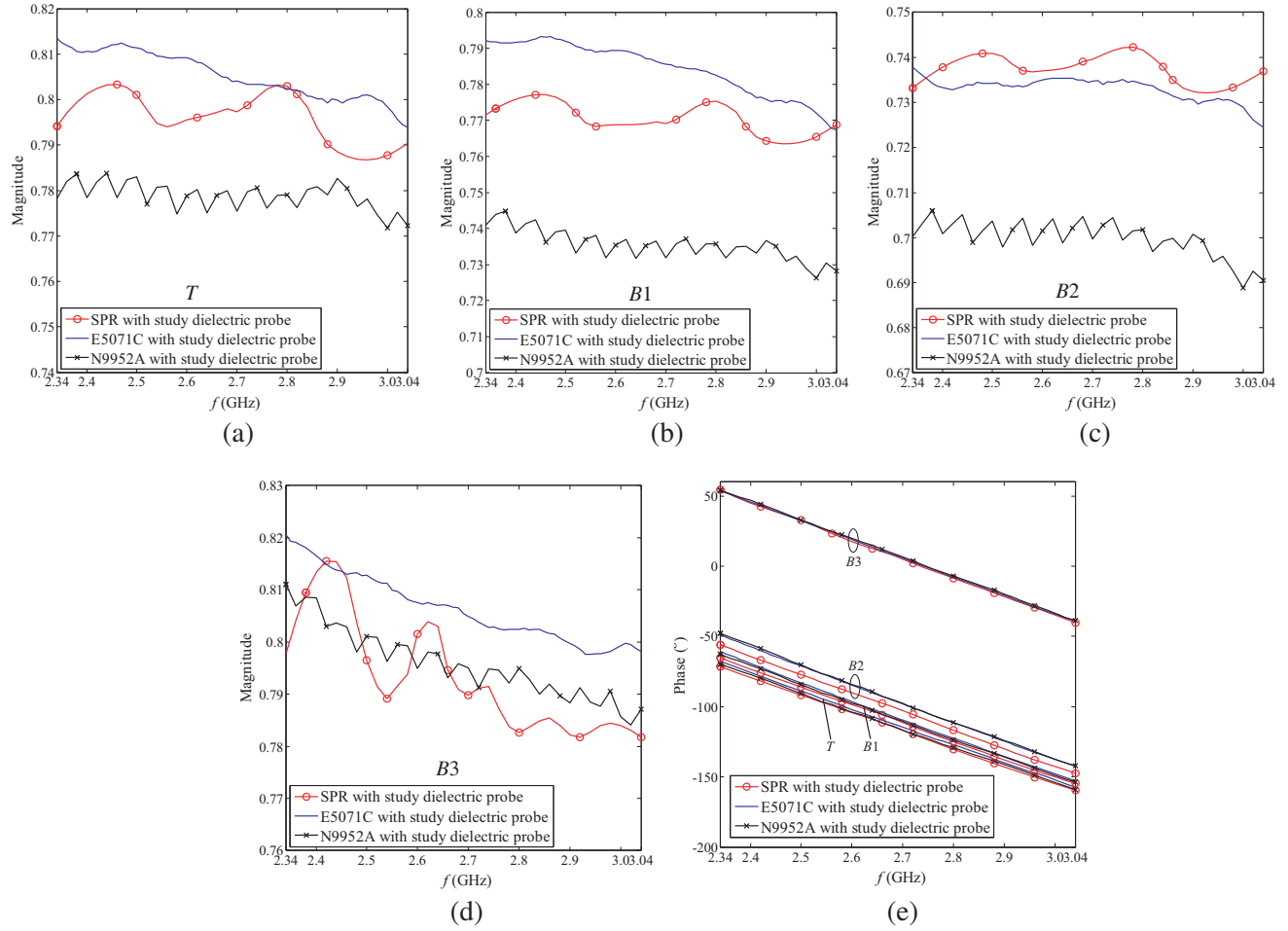
Figure 11. Measurement, (a)–(d) magnitude, (e) phase of SPR, E5071C VNA and N9952A VNA with three normal ($B1$, $B2$, and $B3$) and tumor breast tissues (T).

The maximum errors between the actual measured and reference phases for samples T, $B1$, $B2$, and $B3$ are 3.71°, 4.50°, 4.94° and 1.56°, respectively. On the contrary, the reference and N9952A VNA phases for samples T, $B1$, $B2$, and $B3$ are 1.70°, 1.10°, 0.60°, and 0.77°, respectively. $B3$ sample has the highest phase while T has the lowest phase among all the samples. By observation, all the samples' phases decrease with frequency, due to shorter wavelength as the frequency increases, shown in Figure 11(e). Other than that, the figure also shows that the magnitude of T sample at 2.45 GHz approximately in the range from $-81°$ to $-78°$, while the magnitude value for $B1$ sample is in the range from $-63°$ to $-60°$ at 2.45 GHz. Undoubtedly, the differentiation between tumor and normal synthetic breast tissue samples is differentiable with the phase measurement.

T sample has higher dielectric than $B1$, $B2$, $B3$ samples, while $B3$ sample has the lowet dielectric than T, $B1$ and $B2$ samples. The high dielectric value of T sample was due to high water contents in the sample. Besides, Figure 12(a) shows the dielectric values for T, $B1$, $B2$ and $B3$, which increase with frequency. The figure also shows that the dielectric for T at 2.45 GHz falls in the range from 56.1 to 56.8, while the dielectric for $B1$ is in the range from 47.5 to 48.4 at 2.45 GHz. Obviously, it can be seen that the measurement is capable of differentiating tumorous and normal synthetic breast tissue samples. The mean absolute errors between the predicted and reference loss factors for samples T, $B1$, $B2$, and $B3$ are 0.89, 1.23, 1.77 and 0.50, respectively.

$B3$ has the smallest loss factor, ε_r, since it is a pure and non-polar TX-100 liquid, while T, $B1$, and $B2$ have high loss factors due to certain amount of water in the mixture samples. Indirectly, T, $B1$, and $B2$ indicate higher conductivity properties. In addition, the loss factors for T, $B1$, and $B2$
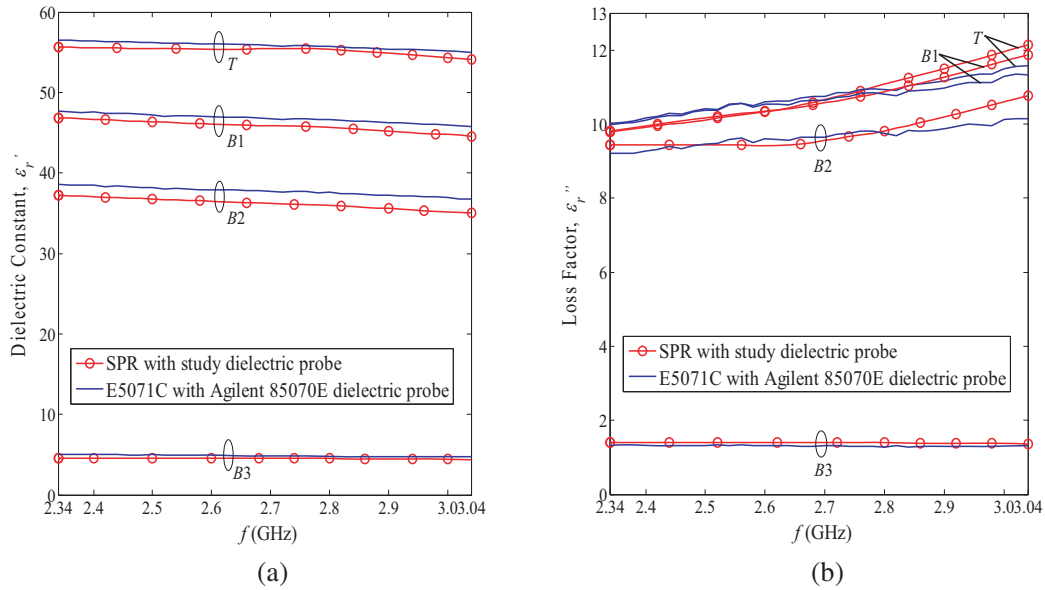
Figure 12. Measurement, (a) dielectric, (b) loss factor of SPR and VNA with three normal ($B1$, $B2$, and $B3$) and tumorous breast tissue (T).

increase with the frequency, except for $B3$. The loss factor traces between T and $B1$ by E5071C VNA with Agilent dielectric probe in Figure 12 seem inseparable at lower frequency but become significantly differentiable at high frequency. Besides, the loss factor measured by SPR with study probe in Figure 12 shows same patterns that may be due to T and $B1$ which mainly contain water. However, $B2$ has much lower loss factor than T and $B1$, due to lower water contents that increase $B2$'s viscosity significantly and "locking" the water of $B2$ from moving freely. The maximum errors between the actual measured and reference loss factors for T, $B1$, $B2$, and $B3$ are 0.56, 0.54, 0.61 and 0.11, respectively.

8. CONCLUSIONS

In this study, the microwave SPR sensor system for synthetic breast tumorous and normal dielectric measurement is successfully fabricated. The chosen architecture for SPR is the ring coupler SPR type because it is simple, physically small, and does not require high precision fabrication process. In addition, the BW of primitive FPRC is improved by 26%, by overlaying a superstrate with an exterior copper layer. Furthermore, the physical size of the enhanced superstrate FPRC is smaller than the one in previous study [11]. Significant distance, t_g, between the metal plate and FPRC that affects $|S_{11}|$ is investigated close to the width, w, of the microstrip copper trace of the FPRC. Maximum absolute mean errors of the linear magnitude and phase measurement of the enhanced superstrate FPRC based SPR are 0.03 and 5.50°, respectively. Other than that, maximum absolute mean error of the predicted dielectric and loss factor are 1.77 and 0.61, respectively. In future, there might be different designs or materials of superstrate that could increase the bandwidth of the FPRC.

REFERENCES

1. Torre, L. A., F. Bray, R. L. Siegel, J. Ferlay, T. J. Lortet, and A. Jemal, "Global cancer statistics 2012," *A Cancer Journal for Clinicians*, 87–108, 2012.

2. Jemal, A., F. Bray, M. M. Center, J. Ferlay, E. Ward, and D. Forman, "Global cancer statistics 2011," *A Cancer Journal for Clinicians*, 69–90, 2011.

3. Speirs, V. and A. Shaaban, "The rising incidence of male breast cancer," *Breast Cancer Research and Treatment*, 429–430, 2009.

4. Jotwani, A. and J. Gralow, "Early detection of breast cancer," *Molecular Diagnosis and Therapy*, 349–357, 2009.

5. Romeo, S., L. Di Donato, O. M. Bucci, I. Catapano, L. Crocco, M. R. Scarfì, and R. Massa, "Dielectric characterization study of liquid-based materials for mimicking breast tissues," *Microwave and Optical Technology Letters*, 1276–1280, 2011.

6. Riblet, G. P. and E. R. B. Hansson, "The use of a matched symmetrical five-port junction to make six-port measurements," *Microwave Symposium Digest*, 151–153, 1981.

7. Lee, K. Y., A. Zulkifly, J. A. Mohamad, K. Y. You, and E. M. Cheng, "Determination of moisture content in oil palm fruits using a five-port reflectometer," *Sensors*, Vol. 11, No. 4, 4073–4085, 2011.

8. Duenas-Jimenez, A. and C. A. Bonilla-Barragan, "On the calibration of a microwave network six-port reflection analyzer," *IEEE Transactions on Instrumentation and Measurement*, Vol. 56, No. 5, 1763–1769, 2007.

9. Lee, K. Y., B. K. Chung, K. Y. You, E. M. Cheng, and A. Zulkifly, "Development of a symmetric ring junction as a four-port reflectometer for complex reflection coefficient measurements," *Radioengineering*, Vol. 24, No. 4, 906–911, 2015.

10. Yao, J. J. and S. P. Yeo, "Six-port reflectometer based on modified hybrid couplers," *IEEE Transactions on Microwave Theory and Techniques*, Vol. 56, No. 2, 493–498, 2008.

11. Staszek, K., J. Sorocki, P. Kaminski, K. Wincza, and S. Gruszczynski, "A broadband 3 dB tandem coupler utilizing right/left handed transmission line sections," *IEEE Microwave and Wireless Components Letters*, Vol. 24, No. 4, 236–238, 2014.

12. Julrat, S., M. Chongcheawchamnan, T. Khaoraphapong, and I. D. Robertson, "Analysis and design of a differential sampled-line six-port reflectometer," *IEEE Transactions on Microwave Theory and Techniques*, Vol. 61, No. 1, 244–255, 2013.

13. Judah, S. K. and M. D. Judd, "Direct synthesis of the matched symmetric five-port junction from its scattering matrix," *IEE Proceedings H — Microwaves, Antennas and Propagation*, Vol. 133, No. 2, 95–98, 1986.

14. De-Ronde, F. C., "Octave-wide matched symmetrical, reciprocal, 4- and 5 ports," *Microwave Symposium Digest*, 521–523, 1982.

15. Yeo, S. P., T. S. Yeo, and K. M. Ng, "First-order eigenmode analysis of symmetrical five-port microstrip ring coupler," *Microwave and Optical Technology Letters*, Vol. 2, No. 3, 91–94, 1989.

16. Dueñas-Jiménez, A., A. Serrano-Santoyo, and F. J. Mendieta, "On the synthesis of some ring junctions for six-port measurement applications," *Microwave and Optical Technology Letters*, Vol. 5, No. 11, 559–563, 1992.

17. Kim, D. I., K. Araki, and Y. Naito, "Properties of the symmetrical circuit and its broad-band five-port design," *IEEE Transactions on Microwave Theory and Techniques*, Vol. 32, No. 1, 51–57, 1984.

18. Yeo, S. P. and F. C. Choong, "Matched symmetrical five-port microstrip coupler," *IEEE Transactions on Microwave Theory and Techniques*, Vol. 49, No. 8, 1498–1500, 2001.

19. Pozar, D. M., *Microwave Engineering*, 4th Edition, Wiley, 2004.

20. Potter, C. and A. Bullock, "Nonlinearity correction of microwave diode detectors using a repeatable attenuation step," *Microwave Journal*, Vol. 36, 272, 274, 277–279, 1993.

21. Engen, G. F., "Calibrating the six-port reflectometer by means of sliding terminations," *IEEE Transactions on Microwave Theory and Techniques*, Vol. 26, No. 12, 951–957, 1978.

22. Wiedmann, F., B. Huyart, E. Bergeault, and L. Jallet, "A new robust method for six-port reflectometer calibration," *IEEE Transactions on Instrumentation and Measurement*, Vol. 48, No. 5, 927–931, 1999.

23. Stumper, U., "Finding initial estimates needed for the engen method of calibrating single six-port reflectometers," *IEEE Transactions on Microwave Theory and Techniques*, Vol. 38, No. 7, 946–949, 1990.

24. Neumeyer, B., "A new analytical method for complete six-port reflectometer calibration," *IEEE Transactions on Instrumentation and Measurement*, Vol. 39, No. 2, 376–379, 1990.

25. Potter, C. M. and G. Hjipieris, "A robust six- to four-port reduction algorithm," *Microwave Symposium Digest*, 1263–1266, 1993.

26. You, K. Y., *RF Coaxial Slot Radiators: Modeling, Measurements and Applications*, 1st Edition, Artech House, 2015.

27. Gregory, A. P. and R. N. Clarke, "Tables of the complex permittivity of dielectric reference liquids at frequencies up to 5 GHz," *NPL Rep. CETM*, Vol. 33, 2001.